UCLA
UCLA Previously Published Works

Title

Atmospheric Humidity Underlies Irreproducibility of Formamidinium Lead Iodide Perovskites

Permalink

Journal

ISSN

Authors

Park, Keonwoo
Tan, Shaun
Kodalle, Tim
et al.

Publication Date

DOI

Copyright Information

Peer reviewed

Atmospheric humidity underlies irreproducibility of formamidinium lead iodide perovskites

Keonwoo Park[a], Shaun Tan[b], Tim Kodalle[c], Do-Kyoung Lee[d], Maged Abdelsamie[e], Ji-Sang Park[a], Joo-Hong Lee[a], Sung-Kwang Jung[a], Jeong Hoon Ko[f], Nam-Gyu Park[d], Carolin M. Sutter-Fella[c,*], Yang Yang[b,*], and Jin-Wook Lee[a,h,*]

K. Park, J.-S. Park, J.-H. Lee, S.-K. Jung, J.-W. Lee

[a]Department of Nano Engineering and Department of Nano Science and Technology, SKKU Advanced Institute of Nanotechnology (SAINT), Sungkyunkwan University, Suwon 16419, Republic of Korea

[h]SKKU Institute of Energy Science & Technology (SIEST), Sungkyunkwan University, Suwon 16419, Republic of Korea

E-mail: jw.lee@skku.edu

S. Tan, Y. Yang

[b]Department of Material Science and Engineering, University of California Los Angeles, CA, 90095, USA

E-mail: yangy@ucla.edu

T. Kodalle, C. M. Sutter-Fella

[c]Molecular Foundry, Lawrence Berkeley National Laboratory, Berkeley, CA, 94720, USA

E-mail: csutterfella@lbl.gov.

D.-K. Lee, N.-G. Park

[d]School of Chemical Engineering, Sungkyunkwan University, Suwon 16419, Republic of Korea

M. Abdelsamie

[e]Materials Sciences Division, Lawrence Berkeley National Laboratory, Berkeley, CA, 94720, USA

J. H. Ko

[f]Arnold and Mabel Beckman Laboratory of Chemical Synthesis, Division of Chemistry and Chemical Engineering California Institute of Technology Pasadena, CA, 91125, USA

35

Abstract

Metal halide perovskite solar cells (PSCs) are infamous for their batch-to-batch and lab-to-lab irreproducibility in terms of stability and performance. Reproducible fabrication of PSCs is a critical requirement for market viability and practical commercialization. PSC irreproducibility plagues all

40 levels of the community; from institutional research laboratories, start-up companies, to large established corporations. In this work, we unravel the critical function of atmospheric humidity to regulate the crystallization and stabilization of formamidinium lead triiodide ($FAPbI_3$) perovskites. We demonstrate that the humidity content during processing induces profound variations in perovskite stoichiometry, thermodynamic stability, and optoelectronic quality. Almost counterintuitively, we

45 show that the presence of humidity is perhaps indispensable to reproduce phase stable and efficient $FAPbI_3$-based PSCs.

1. Introduction

For metal halide perovskite solar cells (PSCs), their subpar operational durability, module scalability, and material toxicity (lead-containing) are challenges often brought up as the major barriers hindering practical commercialization and widespread adoption. The poor reproducibility of PSCs has been relatively overlooked, but negatively impacts institutional research laboratories, start-up companies, and large established corporations all alike. From a commercial standpoint, PSC irreproducibility detrimentally impedes quality control and reduces production yield and thus overall profit margins. Identifying and controlling process variability is thus a crucial consideration for PSCs to become market viable.

Since 2018, nearly all record-breaking, high-performance PSCs (single junction) have been based on formamidinium lead triiodide ($FAPbI_3$) as main component of the absorber layer, often incorporated with excess methylammonium chloride (MACl) which is added for crystallization control.[1, 2] Browsing through the literature, it becomes obvious that many variations exist in the optoelectronic quality, performance, and operational stability of these PSCs reported by different labs (**Table S1, Supporting information**).[3-17] For example, the reported bandgaps show a spread between ~1.48-1.55 eV for the supposedly identical $FAPbI_3$ composition.[1, 3-7, 18] Simultaneously, different groups have reported perovskite fabrication and processing protocols under different atmospheric conditions (**Table S1, Supporting information**).

Owing to the hygroscopic nature of the polar aprotic solvents and ionicity of the component precursors, the perovskite crystallization may intrinsically be affected by the atmospheric humidity content. Previous studies have shown that the presence of water and fabrication under controlled humidity conditions may confer benefits for both the prototype $MAPbI_3$[19-23] and $FAPbI_3$ perovskites.[11, 24-26] While these studies have analyzed the beneficial effects of humidity on perovskites and often concluded with "defect-healing effects"[23, 25], their observations have been largely limited to the optoelectronic quality of perovskites and have relied predominantly on theoretical assumptions. As such, the impact of humidity on $FAPbI_3$ formation and its potential implications for the reproducibility of high-performance PSCs remains a relatively unexplored area of research within the perovskite community.[27] Moreover, the crystallization thermodynamics and kinetics of $FAPbI_3$ are known to be distinct from other perovskites. Most critically, the photo-active α-$FAPbI_3$ perovskite phase is thermodynamically metastable at room temperature, and thus, an effective stabilizer such as MACl is essential to fabricate a phase-pure and stable α-$FAPbI_3$ film. Nevertheless, the effect of humidity (if any) on $FAPbI_3$ formation with such a stabilizer, and how this links back to the reproduction of current high-performance PSCs, has largely been unexplored in the community.

Herein, we utilized *in-situ* capabilities to monitor the perovskite formation and crystallization dynamics under controlled atmospheric environments. We report on the crucial roles of the atmospheric humidity content to affect the stoichiometry, thermodynamic stability, and optoelectronic quality of $FAPbI_3$ perovskites. Thermogravimetry coupled with differential thermal analysis and mass spectroscopy (TG-DTA/MS) provide insights into the physical mechanisms underlying the variations. We show that the presence of atmospheric humidity is perhaps indispensable during processing, and fundamentally underlies the reproducibility of phase stable and high performance $FAPbI_3$ PSCs. This work paves the way in understanding processing control to fabricate reproducible PSCs, a critical hurdle that must be resolved before commercialization of the technology.

2. Results and discussion

2.1 Initial nucleation from solution

Figure 1a illustrates the $FAPbI_3$ film fabrication process. We first investigated the perovskite crystallization dynamics from solution during spin-coating at room temperature in different atmospheres using *in-situ* photoluminescence (PL) (**Figure 1b-d**). Upon antisolvent (diethyl ether) application at ~20 s, strong PL signals emerged owing to the formation of the perovskite and/or intermediate phases. For $FAPbI_3$ without MACl (hereafter denoted as the pristine film) fabricated under a humid atmosphere (50±5% RH, **Figure 1b**), a broad PL peak spanning from 450 to 650 nm can likely be ascribed to the formation of the non-perovskite δ-$FAPbI_3$ "yellow" phase and/or solvent complex phases (selected individual spectra are given in **Figure S1**, **Supporting information**)[28], as verified by the X-ray diffraction (XRD) patterns of the as-spun films (**Figure S2, Supporting information**). For $FAPbI_3$ with MACl added (40 mol% unless otherwise stated[6]), a strong initial broad asymmetric peak around 700 nm immediately appears after antisolvent application (**Figure 1c and S5d, Supporting information**), but rapidly decreases in intensity and almost completely disappears within a short time. This PL peak is possibly related to the metastable formation of the initial nuclei of the α-$FAPbI_3$ "black" phase[29], indicating that MACl incorporation enabled the initial formation of the perovskite phase at room temperature even without annealing treatment. However, the peak emission originating from the δ-$FAPbI_3$ phase becomes dominant, while the α-$FAPbI_3$ phase can be seen to be thermodynamically unstable at this stage (**Figure S3** and **Note S1, Supporting information**). The more rapid dissipation kinetics of the initial nuclei of α-$FAPbI_3$ are observed to occur with increasing humidity, as evidenced by the additional *in-situ* PL data set obtained at various

4

controlled humidity levels (**Figure S4 and Figure S5, Supporting information**). In contrast, for the film of FAPbI$_3$ with MACl excess fabricated under a dry atmosphere (N$_2$ atmosphere, <0.1ppm for H$_2$O and O$_2$ unless otherwise stated) (**Figure 1d**), an intense and asymmetric PL peak appeared around 740 nm immediately upon antisolvent application, and without any trace of a δ-FAPbI$_3$ phase emission at lower wavelength. The PL peak red-shifted and intensified with time, implying that the α-FAPbI$_3$ phase can be formed and remained stable under a dry atmosphere, even at room temperature. This is further evidenced by comparing the XRD patterns of the films (**Figure S2, Supporting information**). The PL peak red-shifting with time is probably associated with the growth of the α-FAPbI$_3$ phase beginning from quantum-confined nanocrystalline nuclei owing to a lowered critical Gibbs free energy under a dry atmosphere (**see Note S1** and **Figure S3, Supporting information**)[29-32]. Highly luminescent but amorphous precursor clusters cannot be excluded as an alternative explanation. Additional observations indicate that the PL signal from both the α-phase and δ-phase emerged during the spin-coating process of pristine FAPbI$_3$ (without MACl) under dry atmospheric conditions, indicating that the perovskite α-phase cannot be fully stabilized under a dry atmosphere without MACl (**Figure S1, Supporting information**). All films were subsequently annealed at 150°C under a dry atmosphere to trigger the full phase conversion to the α-FAPbI$_3$ perovskite phase (**Figure S2b, Supporting information**). The film spin-coated fabricated under a dry atmosphere demonstrated the highest crystallinity with dominant (001) and (002) peaks ascribed to the cubic α-FAPbI$_3$ phase. Scanning electron microscopy (SEM) also indicates that the surface grain size distribution was most enhanced for the film spin-coated under a dry atmosphere (**Figure S6, Supporting information**). Furthermore, we have fabricated devices based on the provided spin coating environments to compare the performance to confirm the detrimental effects of humidity (**Figure S7, Supporting information**). Devices with perovskite spin coated under humidity environment exhibited lower Jsc and poor device efficiency compared to the devices spin coated under dry atmosphere, which is consistent with our observation on the grain size and crystallinity tendency (**Figure S2 and S6**).
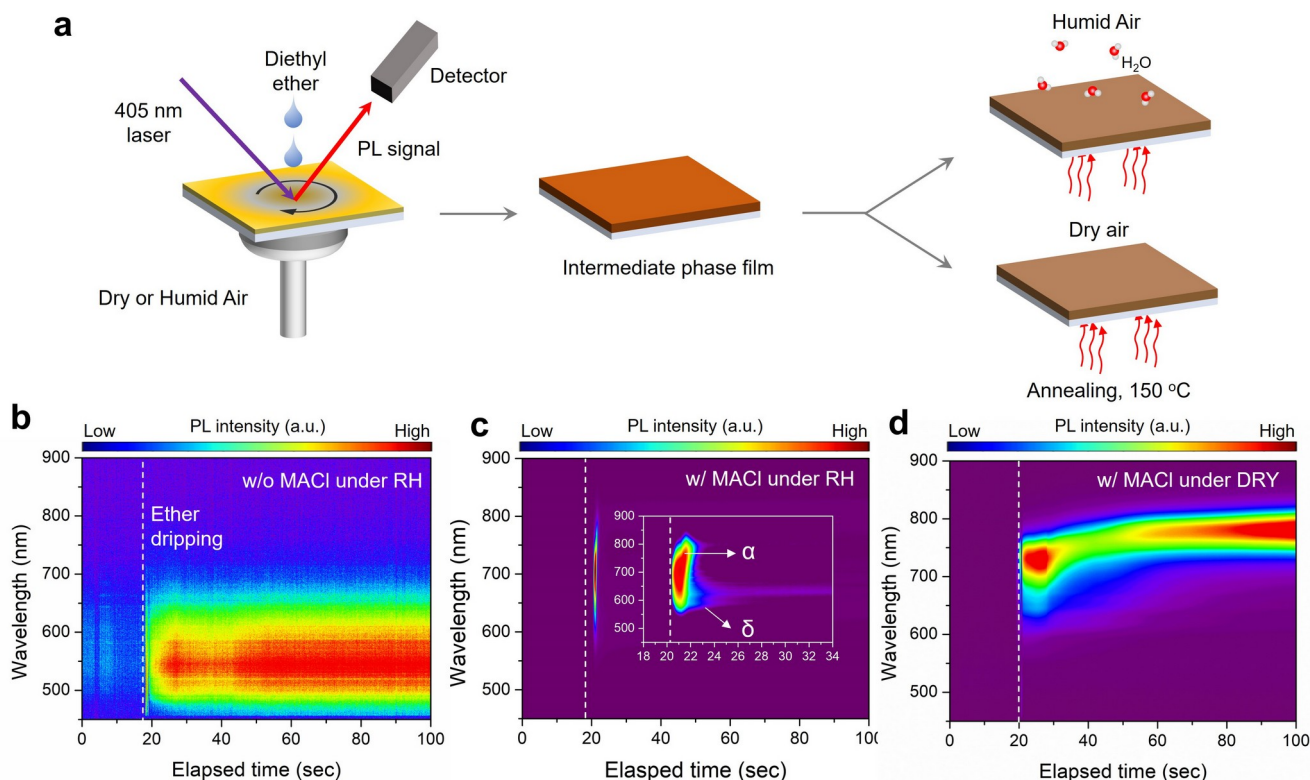
Figure 1. *In-situ* investigation on formation of FAPbI$_3$ films. (a) Schematic illustration of the FAPbI$_3$ thin film fabrication process under different atmospheric conditions. (b-d) *In-situ* photoluminescence (PL) spectra measured during the nucleation process from solution under 50%±5% relative humidity (RH) of the (b) pristine film and (c, d) films with the addition of 40 mol% excess MACl measured under (c) 50±5% RH or (d) dry atmosphere with 0% RH. The in-set PL spectra in (c) illustrates the rapid dissipation of the formed α-FAPbI$_3$ nuclei within short time duration of spin-coating.

2.2 Phase stability and optoelectronic quality of FAPbI$_3$

We further investigated the effect of humidity during the film thermal annealing process. Based on our observations discussed in **Figure 1**, our subsequent studies focused only on the FAPbI$_3$ film with MACl spin-coated under a dry atmosphere. We now varied the thermal annealing atmosphere, under either a dry atmosphere (N$_2$ atmosphere, H$_2$O and O$_2$ < 0.1 ppm, hereafter denoted as FAPbI$_3$-DRY); or humid atmosphere at 30±5% RH (hereafter denoted as FAPbI$_3$-RH). We first compared the ambient environmental stability of the films in **Figure 2a** and **2b**. In striking contrast, the FAPbI$_3$-DRY film was nearly bleached completely after just 24 h storage under ambient conditions (**Figure 2a**), while the FAPbI$_3$-RH film remained barely changed (**Figure 2b**). This is consistent with the XRD patterns of the corresponding films in **Figure 2c**, where the FAPbI$_3$-DRY film can be seen to have mostly phase degraded into the δ-phase after 24 h in ambient. The relatively poor phase stability of the FAPbI$_3$-DRY

film was also observed when the film is stored in a N_2-filled (< 0.1ppm H_2O) glovebox for three weeks, implying that the FAPbI$_3$-DRY film intrinsically experiences more severe phase instability (**Figure S8a** and **S8b, Supporting information**). Accelerated degradation of the FAPbI$_3$-DRY film under ambient air can be attributed to ingress of humidity into FAPbI$_3$[33, 34] which further decreases the activation energy for catalyzing the phase degradation process (**Figure S9, Supporting information**). Steady-state and time-resolved photoluminescence (PL) spectroscopy (**Figure 2d and 2e**) show that the PL intensity of the FAPbI$_3$-RH film (9.7×10^6) was over two orders of magnitude higher than that of the FAPbI$_3$-DRY film (8.8×10^4). Moreover, the different emission peak positions (806 nm for FAPbI$_3$-RH, 798 nm for FAPbI$_3$-DRY) provided the first evidence that the film compositions were different as a result of the annealing atmosphere (*vide infra*). The time-resolved PL decay profiles of the films were fitted to a double exponential decay model. The fitted parameters are summarized in **Table S2, Supporting information**. The relatively smaller proportion and longer fast decay (τ_1) time constant for the FAPbI$_3$-RH film imply a lesser degree of trap-mediated non-radiative recombination of charge carriers, compared to the FAPbI$_3$-DRY film.[35-37] Furthermore, the slow decay (τ_2) time constant for the FAPbI$_3$-RH film (1,076.6 ns) was significantly enhanced as compared to the FAPbI$_3$-DRY film (359.1 ns). Resultingly, the average PL lifetime (τ_{ave}) for the FAPbI$_3$-RH film (1072.1 ns) was more than 156.6% prolonged relative to that of FAPbI$_3$-DRY film (417.7 ns).

Space-charge-limited current (SCLC) measurements were conducted to investigate the trap density (N_t) in the films (**Figure 2f**). The FAPbI$_3$-RH film had a lower trap-filling voltage (V_{TFL}, 0.218 V) than that of the FAPbI$_3$-DRY film (0.284 V). The calculated N_t value significantly reduced from 3.22×10^{15} cm^{-3} (FAPbI$_3$-DRY film) to 1.28×10^{15} cm^{-3} (FAPbI$_3$-RH film), consistent with the higher PL intensity and longer carrier lifetime of the FAPbI$_3$-RH film. In **Figure S10** and **Table S3, Supporting information**, the photovoltaic parameters of the proof-of-concept PSC devices based on the FAPbI$_3$-DRY and FAPbI$_3$-RH films are presented. The photovoltaic parameters of the FAPbI$_3$-RH devices can all be seen to be higher. In particular, the average open-circuit voltage (V_{OC}) of the FAPbI$_3$-RH devices (1.12± 0.01 V for reverse scan) was improved by 13.1% relative to that of FAPbI$_3$-DRY devices (0.99±0.01 V for reverse scan). Current density-voltage (J-V) curves and stabilized power output (SPO) data for the best-performing devices are demonstrated in **Figure S10b and c, Supporting information**. The SPO of the FAPbI$_3$-RH device was 21.34%, which is improved by 19% relative to that of the FAPbI$_3$-DRY device (17.93%, *Note that no surface treatment or additive has been applied for all devices just discussed*). **Figure S11, Supporting information**, further shows the external quantum efficiency (EQE) spectra of the devices. The improved integrated short-circuit current density (J_{SC}) of the FAPbI$_3$-RH device (23.12 mA/cm^2) compared to the FAPbI$_3$-DRY device (22.20 mA/cm^2) was well correlated

with the J_{SC}s measured from the J-V measurements (<5% discrepancy). From the normalized EQE spectra (**Figure S11b, Supporting information**), a slightly red-shifted absorption edge of the FAPbI$_3$-RH device is in line with the observations from the PL peak position measurements. The best-performing FAPbI$_3$-RH device with surface passivation demonstrated PCE of 23.81% under reverse scan (22.80% under forward scan, **Figure S12, Supporting information**). To check if this observation is applicable to different processes and compositions, we further fabricated devices by the anti-solvent free, scalable D-bar coating process. We also used a different composition of (FAPbI$_3$)$_{0.95}$(CsPbBr$_3$)$_{0.05}$ with 30 mol% MACl excess.[12] We employed an air-knife assisted D-bar coater as shown in **Figure S13a, Supporting information** (details in the experimental section). Notably, the device fabricated using the D-bar coating process exhibited consistent improvements across all photovoltaic parameters when annealed under a humid environment compared to a dry atmosphere (**Figure S13** and **Table S4, Supporting information**). Altogether, we supposed that humidity during the film annealing process has beneficial effects on the optoelectronic quality of the perovskite films.
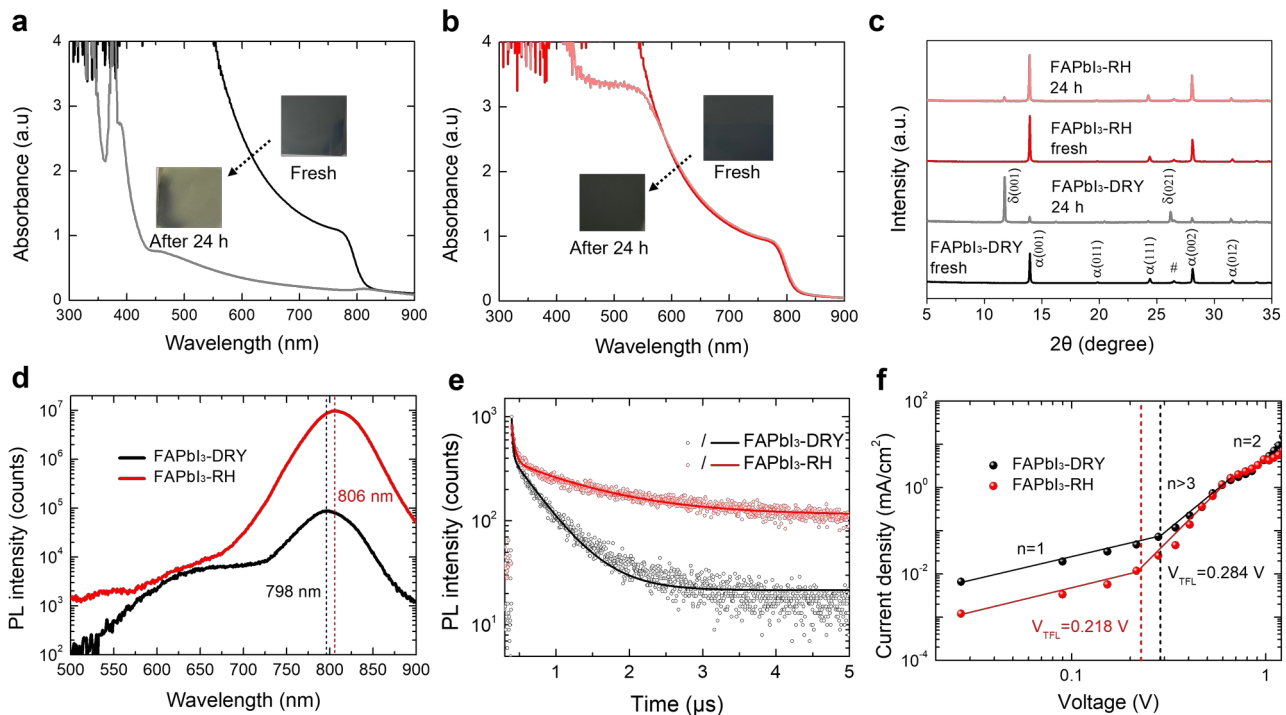

Figure 2. Phase stability and optoelectronic properties of α-FAPbI$_3$ films. (a, b) UV-visible absorption spectra of fresh and aged FAPbI$_3$ films annealed under a (a) dry atmosphere (RH 0%, H$_2$O<1 ppm) or (b) humid atmosphere (RH 30±5%) for 10 min. The films were aged in ambient for 24 h (RH 30± 5%,). (c) X-ray diffraction (XRD) patterns of the corresponding fresh and aged films. (d) Steady-state photoluminescence (PL) spectra, (e) time-resolved PL decay profiles, and (f) space-charge-limited current measurements of the FAPbI$_3$ films annealed under a dry or humid atmosphere (RH30±5%) for 30 min.

2.3 Perovskite crystallization and grain growth during thermal annealing

To understand the implied composition difference between the films, we subsequently monitored the absorption of the $FAPbI_3$-DRY and $FAPbI_3$-RH films *in-situ* during the thermal annealing process (**Figure 3a-d**). A home-built chamber with atmosphere and humidity control was used for the measurements (**Figure S14, Supporting information**). Obvious differences in the absorptance evolution can be observed for the films, particularly around the 600 nm to 800 nm range. From **Figure 3e**, the $FAPbI_3$ with 40mol% excess MACl compared to the pristine $FAPbI_3$ film (without MACl) experienced a blue-shifted absorption edge in addition to reduced absorptance between 600 nm to 800 nm, before prolonged annealing, probably due to formation of the $FA_{1-x}MA_xPbI_{3-y}Cl_y$ intermediate phase (x>y, **Note S2, Supporting information**).[6] Therefore, we postulate that the progressive absorptance enhancement with time between 600 nm to 800 nm (red arrows in **Figure 3c** and **d**) is associated with MACl vaporization during thermal annealing. For the $FAPbI_3$-RH film, the absorptance in this wavelength region rapidly saturated in a few tenths of seconds, whereas that of the $FAPbI_3$-DRY film exhibited a significantly delayed absorptance evolution (inset of **Figure 3d**). In addition, an obvious red-shifting of the absorption edge simultaneously occurred during thermal annealing for the $FAPbI_3$-RH film (**Figure 3d**), whereas slight blue-shift of the absorption edge was observed for the $FAPbI_3$-DRY film. For the $FAPbI_3$-RH film, the vaporization of MACl should induce conversion of the intermediate $FA_{1-y}MA_yPbI_{3-x}Cl_x$ to $FAPbI_3$, resulting in red-shift of absorption edge. On the contrary, such a reaction is relatively not active for the $FAPbI_3$-DRY film, and thus incorporation of MACl into the lattice (particularly MA^+, i.e. x<y) might induce the observed slight blue shift in absorption edge. Based on this, we conjecture that humidity beneficially facilitates the vaporization of MACl during the thermal annealing of $FAPbI_3$. This is also consistently supported by subsequent *in-situ* absorptance measurements under different atmospheric humidity contents, where a higher humidity content progressively promoted the absorptance enhancement and the red-shifting of the absorption edge towards longer wavelengths (**Figure S15** and **S16, Supporting information**). Regardless of different humidity levels, Humidity-assisted annealing consistently resulted in higher device performance, particularly in terms of open-circuit voltage (V_{OC}) and current density (J_{SC}), across all humidity levels, where the most notable improvement was observed at a humidity level of RH 30% (**Figure S17** and **Table S5, Supporting information**). The steady-state and time-resolved PL data was correlated with observed trend in device performance with different humidity levels (**Figure S18** and **Table S6, Supporting information**). At this stage, we speculate that the more effective vaporization of MACl additive with higher RH might facilitate formation of less defective $FAPbI_3$ films. However, too high

humidity (RH 50%) might damage the perovskite film. Indeed, exceptional absorptance change with the RH 50% was observed in **Figure S16, Supporting information**. Still, it is important to note that the optimal humidity level for perovskite fabrication may vary depending on the choice of precursor composition and fabrication parameters (e.g. solvent, composition, additives, annealing temperature and time, etc). Importantly, for pristine $FAPbI_3$ without MACl, such dynamic evolution of the absorptance and red-shifting were not observed regardless of the atmospheric humidity levels, indicating that the observed absorptance evolution may be primarily due to MACl vaporization (**Figure S19, Supporting information**).

We also monitored the XRD patterns of the films with annealing time (**Figure 3f** and **Figure S20, Supporting information**). During the annealing process, the α (001) and α (002) peaks gradually shifted toward lower 2θ angles, indicating expansion of the α-$FAPbI_3$ lattice. In consideration of the smaller ionic radii of MA^+ and Cl^- as compared to FA^+ and I^-, respectively, the gradual peak shifts toward lower 2θ can be associated with the vaporization of MACl from $FA_{1-x}MA_xPbI_{3-y}Cl_y$, accompanied by the incorporation of FA^+ and I^-.[6] Particularly, comparing the same annealing times, the $FAPbI_3$-RH film experienced larger 2θ shifts towards lower angles (**Figure 3f**, **Figure S21** and **Table S7, Supporting information**), complementing the *in-situ* absorptance results that the volatilization of MACl is accelerated by humidity. As shown in the surface SEM images in **Figure S22, Supporting information**, the grain sizes of the films were comparable regardless of the different annealing atmospheres, implying that the observed difference in phase stability and optoelectronic properties is due to inherent differences in the film composition associated with the volatilization of MACl.

Linking back to the observed aggravated phase instability (**Figure 2a and 2b**), we investigated perovskite films with compositions $FA_{1-x}MA_xPbI_3$ and $FAPb(I_{1-y}Cl_y)_3$ (**Figure S23, Supporting information**). For $FA_{1-x}MA_xPbI_3$, a single perovskite phase can be formed even up to x=0.40, whereas for $FAPb(I_{1-y}Cl_y)_3$, PbI_2 and δ-$FAPbI_3$ emerged even for incorporation levels as low as y=0.02. This observation can likely be explained using tolerance factor considerations[1, 38, 39]; while MA^+ beneficially reduces the tolerance factor of $FAPbI_3$ to stabilize the α-phase, Cl^- incorporation adversely increases the tolerance factor and facilitates defect generation to aggravate the phase instability of α-$FAPbI_3$ (**Figure S24, Note S2** and **S3, Supporting information**). Therefore, most of the added MA^+ substitute for FA^+ in the lattice, while only a small fraction of Cl^-, if any at all, can be incorporated into the cubic perovskite lattice, resulting in a precipitation of excess FACl and FAI as follows:
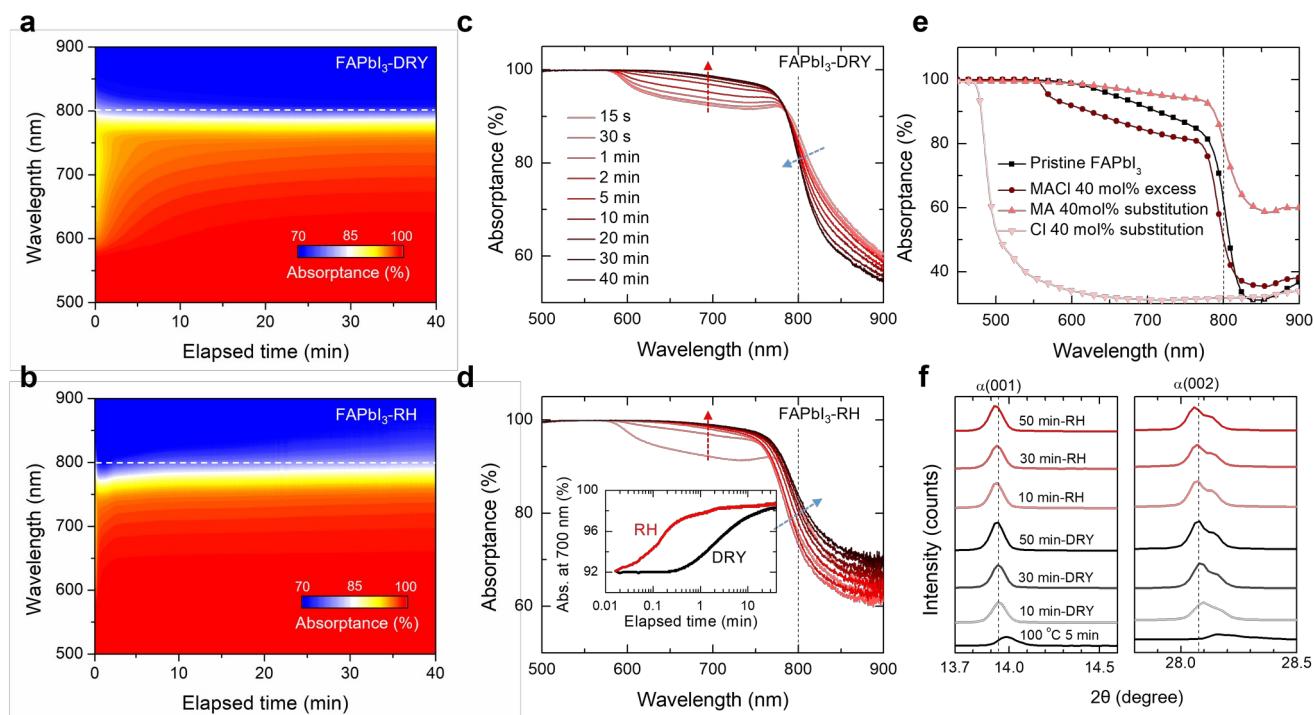
$$FAPbI_3 + y\ MACl \rightarrow FA_{1-y}MA_yPbI_{3-x}Cl_x + (y-x)\ FACl + xFAI \qquad (y>x)$$
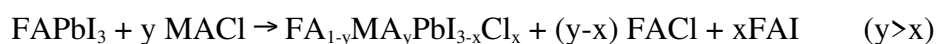
Figure 3. In-situ absorptance and XRD of FAPbI$_3$ during thermal annealing. (a, b) *In-situ* absorptance spectra of the FAPbI$_3$ films annealed under a (a) dry atmosphere or (b) 30±5% relative humidity (RH). (c, d), Selected absorptance spectra of the films annealed under a (c) dry atmosphere or (d) 30±5% RH. The color coding for the time legends for (c) and (d) are the same. Inset in d shows the absorptance evolution at 700 nm. (e) Absorptance spectra of the pristine FAPbI$_3$ film and FAPbI$_3$ with different substituents, after annealing at 150 °C for 30 s. (f) X-ray diffraction (XRD) patterns of films at different annealing times under a dry atmosphere or 30±5% RH.

We thus hypothesize that the excess FACl and/or FAI generated in the film is responsible for the phase instability and poor optoelectronic quality of the FAPbI$_3$-DRY film. Subsequent experiments to incorporate excess FAI or FACl into pristine FAPbI$_3$ (without MACl) were performed to verify this hypothesis (**Figure S25, Supporting information**). Notably, we observed that a phase-pure α-FAPbI$_3$ cannot exist solely with the addition of >10 mol% of excess FACl. After storage under ambient conditions for 24h, the films with excess FAI or FACl underwent nearly complete phase degradation to the δ-phase. Their observed phase stability was even inferior to that of the pristine FAPbI$_3$ film. In our previous study, we showed that excess I$^-$ can generate iodine interstitial defects to accelerate the phase degradation of α-FAPbI$_3$.[40] Similarly, the presence of excess FA$^+$, MA$^+$, I$^-$ and/or Cl$^-$ likely resulted in the formation of interstitial defects, which may have contributed to the observed deterioration of perovskite phase stability.[41] We noted that FA$_i$+I$_i$, FA$_i$+Cl$_i$, MA$_i$+ Cl$_i$, and MA$_i$+I$_i$ split interstitial defect complexes have formation energies of 0.562 eV, 0.300 eV, 0.480 eV, and 0.449 eV,
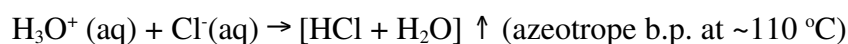
11

respectively, which are higher than that of halide Frenkel pairs (**Figure S26 and S27, Supporting information**) but comparable to other intrinsic point defects.[41] Notably, the defect complex consisting of FA_i and Cl_i exhibited the lowest formation energy, consistent with compositional studies involving excess FAI and FACl in $FAPbI_3$ (**Figure S25, Supporting information),** where the films with excess FACl showed much worse α-phase instability compared to the film with the same amount of excess FAI. Not only does the intrinsic phase stability degrade, but the interaction of the defect with surrounding humidity should further degrade the phase stability of the $FAPbI_3$-DRY film under ambient atmosphere.[42, 43]

2.4 Humidity-catalyzed volatilization of MACl

In **Figure 4a**, time-of-flight secondary ion mass spectrometry (TOF-SIMS) analysis of the $FAPbI_3$-DRY and $FAPbI_3$-RH films was conducted to investigate the residual Cl^- content in the films. The TOF-SIMS 3D image confirmed a lower residual Cl^- content in the $FAPbI_3$ film annealed under a humid atmosphere (line profiles are shown in **Figure S28, Supporting information**). It was noted that the intensity of the Cl^- in the film's bulk region is comparable to that on the top and bottom surfaces, implying incorporation of Cl^- at interstitial and/or lattice sites. The relatively lower Cl^- content observed from the $FAPbI_3$-RH films is consistent with energy-dispersive X-ray (EDX) analysis of the films. Specifically, the EDX analysis revealed negligible Cl content in the $FAPbI_3$-RH films, whereas $FAPbI_3$-DRY showed a noticeable amount of Cl residues, with a concentration of 3.9 mol% (**Figure S29 and Table S8, Supporting information**). As discussed above, we note that $FAPbI_3$ film showed much accelerated phase conversion from α to δ phase even with 1 mol% excess of FAI or FACl in **Figure S25, Supporting information**.

To investigate possible mechanisms, we performed thermogravimetry coupled with differential thermal analysis and mass spectroscopy (TG-DTA/MS) on pure MACl powder in **Figure 4b-e**. We compared the TG-DTA/MS of the completely dry MACl (**Figure 4b** and **4d**) versus MACl exposed to humidity (**Figure 4c** and **4e**). The MS peaks corresponding to MACl were assigned as summarized in **Table S9, Supporting information**.[44-50] Even prior to TG-DTA/MS, we observed that the initially solid MACl powder liquified when exposed to humidity (inset of **Figure 4c**), demonstrating the highly hygroscopic nature of MACl. For the case of the dry MACl powder, the weight loss began at ~234.4°C (endothermic peak in DTA) with simultaneous detection of gaseous fragments such as NH_2^+, NH_4^+, CH_2N^+ and $H^{35}Cl^+$ (MS for the other fragments are included in **Figure S30, Supporting information**). On the other hand, the MACl powder exposed to humidity showed a noticeable initial weight loss

12

starting from ~50°C, with a broad endothermic peak at ~113.2°C. The weight loss can be primarily attributed to the vaporization of water, but notably, MACl also vaporizes simultaneously, as directly evidenced by the detection of the NH_2^+, NH_4^+, CH_2N^+ and $H^{35}Cl^+$ fragments between 50°C and 250°C. Moreover, the additional weight loss and endothermic peaks at higher temperatures occurred at lower temperatures for the MACl powder exposed to humidity (232.0°C and 326.8°C; versus 234.4°C and 334.4°C for the dry MACl powder). We attributed the simultaneous vaporization of water and MACl to a solvation effect by water to generate volatile species as follows:

$$CH_3NH_3Cl\ (s) \rightarrow CH_3NH_3^+\ (aq) + Cl^-\ (aq)$$

$$CH_3NH_3^+\ (aq) + H_2O \leftrightarrow CH_3NH_2\ (g) \uparrow + H_3O^+\ (aq)$$

$$H_3O^+\ (aq) + Cl^-(aq) \rightarrow [HCl + H_2O] \uparrow\ (azeotrope\ b.p.\ at\ \sim110\ °C)$$

First, solid-state MACl absorbs moisture from the atmosphere and dissolves in it. Next, the solvated MA^+ cation is a weak acid, and thus it can transfer a proton to a water molecule to generate an H_3O^+ ion. Although the equilibrium favors the reverse reaction due to the higher basicity of the amine, the proton exchange occurs rapidly and allows some methylamine to evaporate either by itself or together with other neutral water molecules. Finally, H_3O^+ can associate with solvated Cl^- to form HCl, whose boiling point is dependent on composition, but significant evaporation is expected during thermal annealing of the perovskite film at 150°C. The loss of MA^+ (in the form of methylamine) and Cl^- (in the form of hydrochloric acid) is consistent with our TG-DTA/MS results (**Figure 4** and **Figure S30, Supporting information**).
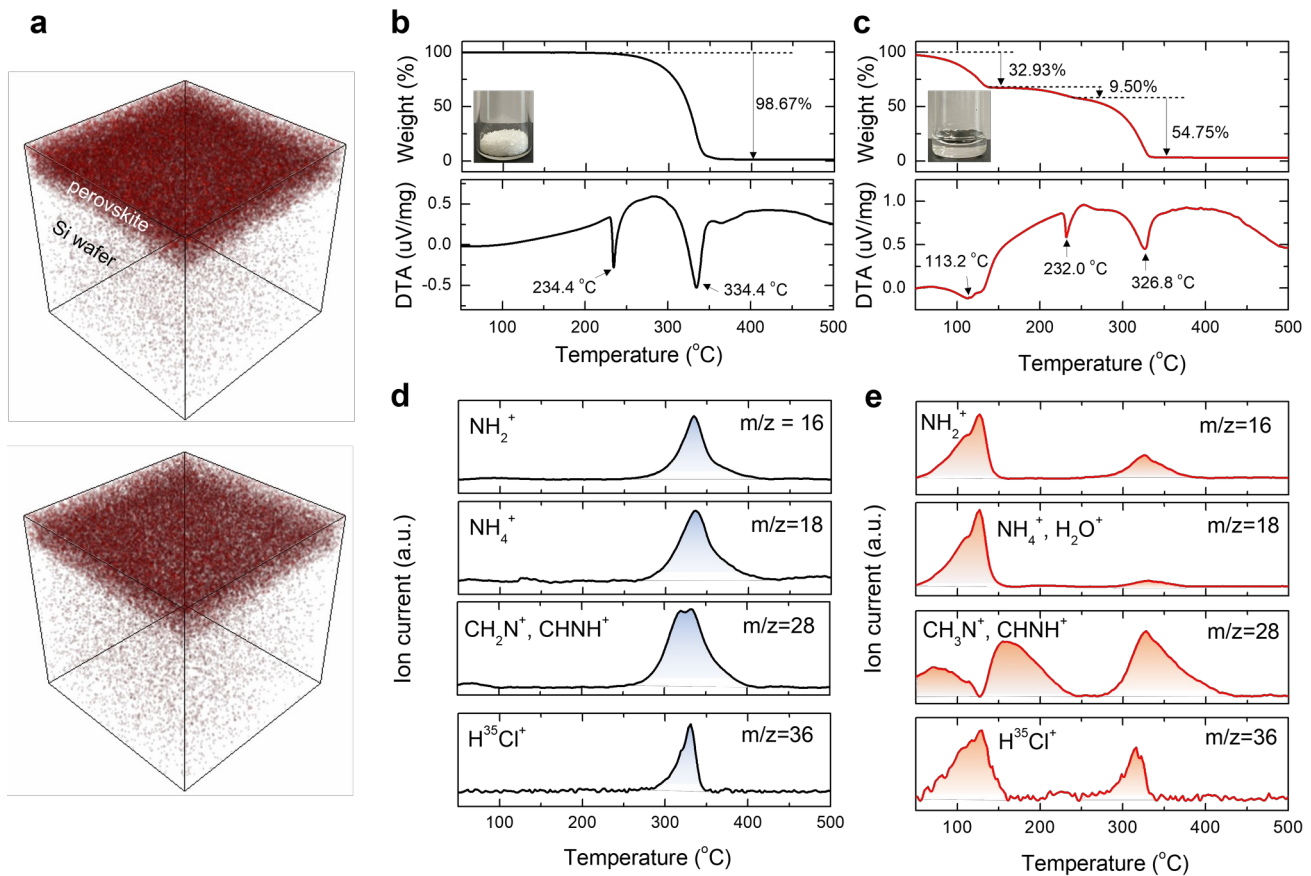
Figure 4. Investigation of residual Cl and its origin. (a) Time-of-flight secondary ion mass spectrometry of Cl anion in FAPbI$_3$ films with 40 mol% excess MACl annealed under dry air (upper panel) and 30% relative humidity (lower panel). Measured area is 40 μm by 40 μm. (b, c) Thermogravimetry coupled with differential thermal analysis and mass spectroscopy (TG-DTA/MS) analysis of (b) dry MACl powder and (c) MACl powder exposed to humidity for 24 h. The arrows in the DTA curves indicate inflection points of the spectra. The heating rate was 5 °C/min, and the measurements were carried out under an Ar atmosphere. (d, e) Temperature dependent MS data of the (d) dry MACl powder and (e) MACl powder exposed to humidity measured during heating. The mass-to-charge ratios (m/z) and corresponding fragments are labeled in each plot.

3   Conclusions

In summary, we performed systematic studies coupled with theoretical calculations to investigate the profound roles of atmospheric humidity to influence the stoichiometry, thermodynamic stability, and optoelectronic quality of FAPbI$_3$ perovskite films with the addition of MACl. We show that humidity destabilizes the initial desirable α-phase perovskite nuclei formation during the spin-coating process. On the other hand, atmospheric humidity content beneficially assists in stabilizing the α-phase perovskite by promoting the vaporization of hygroscopic MACl during the thermal annealing process.

14

Our work demonstrates that careful consideration of the PSC fabrication environment is vital to prevent irreproducibility, and detailed information regarding the fabrication environment needs to be provided to foster the realization of perovskite commercialization.

4 Experimental section

Materials

N,N-Dimethylformamide (DMF, anhydrous, 99.8%), N-Methyl-2-Pyrrolidone (NMP, anhydrous, 99.9%), diethyl ether (>99.7%), chlorobenzene (CB, 99.8%), lithium bis (trifluoromethane sulfonyl)imide (LiTFSI, 99.8%), 4-tert-butyl pyridine (tBP, 98%), acetonitrile (ACN, 99.9%), formamidinium acetate (FAAc, 99%), Lead (II) bromide (PbBr$_2$, >99.999%), 1,3-dimethyl-3,4,5,6-tetrahydro-2(1H)-pyrimidinone (DMPU, > 98%), and Titanium diisopropoxide bis(acetylacetonate) (TiO$_2$, 75 wt.% in isopropanol) were purchased from Sigma Aldrich. Aqueous colloidal tin (IV) oxide solution (SnO$_2$, 15 wt% in H$_2$O) was purchased from Alfa Aesar. 2,2',7,7'-tetrakis(N,N'-di-p-methoxypheneylamine)-9,9'-spirobifluorene (Spiro-MeOTAD) was purchased from Lumtec. Lead (II) iodide (PbI$_2$, 99.99%) was purchased from TCI. Hydrochloric acid (HCl, 35.0–37.0%) was purchased from Samchun Chemicals. Formamidinium iodide (FAI), and methylammonium chloride (MACl) were purchased from Greater Solar. Formamidinium chloride (FACl) was synthesized according to previously reported methods.[51] FTO glass (Pilkington, TEC-8, 8 Ω/sq) was used as the conductive substrate.

Perovskite precursor solution preparation

The FAPbI$_3$ perovskite solution was prepared by mixing 461 mg lead iodide (PbI$_2$, TCI) and 172 mg FA iodide (FAI, Greatcell solar), and 1 mol of NMP in 500 uL of DMF. For the additive engineering of MACl, 40 mol% (27 mg) MACl were added to the FAPbI$_3$ perovskite solution. The Spiro-MeOTAD solution was prepared by mixing 86.8 mg Spiro-MeOTAD, 34 uL tBP, and 20 uL LiTFSI solution (520 mg Li-TFSI dissolved in 1 mL ACN).

Small-area device fabrication

FTO glass was cleaned with detergent, acetone, deionized water, and ethanol for 15 min by ultrasonication. The cleaned FTO glass was then dried with nitrogen gas. The dried FTO glass was further treated with ultraviolet ozone (UVO) for 1 hour. A SnO$_2$ layer was deposited on the FTO substrate by spin-coating the diluted SnO$_2$ solution at 4000 rpm for 20 s, which was annealed at 185 °C for 30 min. The SnO$_2$-coated FTO substrate was then treated again with UVO for 30 min prior to

coating the perovskite layer. The perovskite solutions were spin-coated onto the SnO_2-coated FTO substrate at 4000 rpm for 20 s. Diethyl ether (0.15 mL) was dripped after 10 s during the 20 s rotation. The perovskite films were annealed at 100 °C for 5 min and then annealed at 150 °C for different times under a dry and humid environment. For the best-performing device, octylammonium tosylate surface passivation was applied as described in the previous study.[52] The hole-transporting layer was deposited on the perovskite film by spin-coating the 30 uL Spiro-MeOTAD solution at 3000 rpm for 25 s. A 100 nm Ag electrode was deposited on the Spiro-MeOTAD layer using a thermal evaporator at an evaporation rate of 0.1–0.9 Å/s.

Device fabrication based on D-bar coating

Fluorine-doped tin oxide (FTO)-coated substrates (4.8 cm x 9.6 cm) were cleaned by sonication for 30 min with isopropanol. Before depositing TiO_2 and SnO_2 layers, the substrates were treated by UV/ozone cleaner for 60 min. Compact TiO_2 layer was first coated on FTO substrates, and then SnO_2 layer were deposited on FTO/c-TiO_2 substrates. 0.1M titanium diisopropoxide bis(acetylacetonate) solution diluted in 1-butanol was spin-coated at 4000 rpm for 30 s and then annealed at 125 °C for 15 min on the hot-plate and 450 °C for 30 min in the furnace. For forming SnO_2 layer, the diluted colloidal SnO_2 solution (1:3 volume ratio with deionized water) was spin-coated at 3000 rpm for 30 s and then annealed at 180 °C for 20 min on the hot-plate. 20 mM potassium chloride solution dissolved in deionized water were treated on FTO/TiO_2/SnO_2 substrates by the spin coating process at 3000 rpm for 30 s and then heated at 150 °C for 30 min. Before coating perovskite layers, the substrates were treated by UV/ozone for 30 min. 1.43 M perovskite precursor solution was prepared by dissolving 163.4 mg FAI, 437.9 mg PbI_2, 10.6 mg CsBr, 18.4 mg $PbBr_2$ and 20.3 mg MACl in 639.5 μl DMF and 60.5 μl DMPU. The precursor solution was filtered with 0.2 μm pore size of PTFE-H filter prior to use. To form large-area perovskite layers, we used the D-bar & air-knife coating process. 54 μl perovskite precursor solution was loaded on the substrate and then coated with 3 mm/s coating velocity. Argon gas blowing by air-knife with 2.0 MPa blow pressure was supplied to the wet film. The as-coated films were annealed at 150 °C for different time on the hot-plate under N_2 inert and ambient conditions. Spiro-MeOTAD layer was spin-coated on the perovskite film at 3000 rpm for 30 s, where the spiro-MeOTAD solution was prepared by dissolving 90.9 mg spiro-MeOTAD, 39 μl TBP and 23 μl Li-TFSI solution (520 mg/ml in ACN) in 1 ml chlorobenzene. Au counter electrode was deposited by thermal evaporation with 0.3 Å/s evaporation rate.

Device characterization

Photocurrent density-voltage (J-V) curves were obtained under AM 1.5G 1 sun (100 mW/cm^2) illumination using a solar simulator (Oriel Sol 3A, class AAA) equipped with a 450 W xenon lamp (Newport 6280NS) and Keithley 2400 source meter. The J-V curves of the PSCs were obtained with a scan rate of 0.1V/s from -0.1 V to 1.2 V (forward scan) or 1.2 V to -0.1 V(reverse scan). The light intensity was adjusted using an NREL-calibrated silicon reference solar cell. Pre-conditioning, such as applied bias voltage and light-soaking, was not performed prior to the measurement. The PSCs were measured with a metal mask (aperture area 0.125cm^2) under ambient environment (temperature $\cong$ 25°C, relative humidity $\cong$ 30%). For the best performance PSCs **(Figure S12, Supporting information)**, 150 nm thick MgF$_2$ anti-reflection layer was deposited on the glass side of the FTO substrate. The SPO measurements were performed by measuring photocurrent density at a constant bias voltage 0.935V and 0.802V for FAPbI$_3$-RH and FAPbI$_3$-Dry, respectively. The EQE spectra were obtained using an IPCE system equipped with a 75 W Xenon lamp (USHIO) as a white light source, where the monochromatic beam was generated under DC mode conditions. SEM images were obtained using a field-emission SEM (JSM-7401F).

Material characterization

XRD patterns were obtained using a Rigaku SmartLab SE X-ray diffractometer with monochromatic Cu Kα radiation (λ = 1.5406 Å) at a scan rate of 4°/min. UV-absorption spectra were recorded using a UV-vis spectrometer (Lambda 45, PerkinElmer). Steady-state PL and time-resolved PL decay profiles were measured using a Quantarus-Tau compact fluorescence lifetime spectrometer (Quantaurus-Tau C11367, Hamamatsu) with excitation by a 464 nm laser (PLP-10, Hamamatsu). For SCLC measurement, the device with structure of ITO/Perovskite/Au was used. The N_t is calculated using the equation $V_{TFL} = N_t eL^2/2\varepsilon_0\varepsilon_r$ (e = electric charge, L = thickness of the absorber film (FAPbI$_3$-DRY ~700 nm, FAPbI$_3$-RH ~680 nm), ε_0 = vacuum permittivity, and ε = dielectric constants). TG-DTA/MS was conducted using a simultaneous thermal analyzer at a scan rate of 5 °C/min, heated from 35 to 550 °C under argon flow.

In-situ measurements

In-situ photoluminescence (PL) measurements were acquired during spin-coating and post-annealing on a hot plate. Measurements were performed under controlled atmosphere with a home-built setup as described in previous works [31, 53] using a 405 nm laser diode, a plano-convex lens above the substrate, a 450 nm long-pass filter, and a fiber-coupled Ocean Optics spectrometer (Flame) calibrated by the manufacturer. A maximum power density of ~100 mW/cm^2 was used during the in-situ PL measurements. Spectra were continuously acquired every 100 ms. PL emission spectra were fitted using single Gaussian peak fitting after background counts were accounted for by the spectrometer and Jacobian transformation to the energy scale.[54] Transmission measurements were collected using a fiber coupled with an Ocean Optics spectrometer (Flame) with an integration time of 0.1 s per transmission spectrum. The equation $[A_\lambda = -\log_{10}(T_\lambda)]$ was used to calculate the UV-visible absorption spectra from the transmission spectra, where A_λ is the absorbance at a certain wavelength (λ) and T_λ is the corresponding transmitted radiation. The in-situ UV-visible absorption measurements during spin-coating were performed using a setup described in a previous study. [55] The in-situ UV-visible absorption measurements during thermal annealing were performed using a custom-built heating stage with a hole that allowed transmission measurements [56]. The heating stage was placed in a custom-built chamber with controlled humidity.

Density functional theory calculation

We performed density functional theory calculation using the PBEsol exchange-correlation functional[57] and the projector augmented wave (PAW) pseudo-potential [58], as implemented in the

Vienna ab-initio Simulation Package (VASP) code[59]. The energy cutoff for the plane waves was set to 400 eV, and the atomic structures were fully optimized until the residual forces becomes less than 0.03 eV/Å. Defects were investigated by employing a 192-atoms supercell, and a 2×2×3 *k*-point mesh was used for the Brillouin zone integration.

Supporting Information

Supporting Information is available from the Wiley Online Library or from the author.

Conflicts of interest

There are no conflicts to declare.

Author contributions

J-W.L. conceptualized the idea and designed the experiments. K.P. conducted most of the experiments under supervision of J-W.L. Y.Y. and C.M.S.-F. K.P., S.T. and S-K.J. fabricated the PSCs for characterization of perovskite films under controlled atmospheric humidity. D-K. L. fabricated the large-area PSCs utilizing an air-knife assisted D-bar coater and measured PSCs under supervision of N.-G.P. J-H.L. measured XRD of perovskite films. S.T., T.K., M.A., and K.P. carried out in-situ experiments of perovskite films under supervision of C.M.S.-F. J-S.P. did modeling and interpretation of DFT calculations. J-W.L. and J.H.K. assisted with the data analysis of TG-DTA/MS. K.P. S.T. and

J-W.L. wrote the manuscript, with all corresponding authors supervised and edited the manuscript. All authors contributed feedback and comments on the manuscript.

520

References

[1]   J.-W. Lee, S. Tan, S. I. Seok, Y. Yang, N.-G. Park, *Science* **2022**, 375, eabj1186.

[2]   C. Zhu, C. Wang, P. Zhang, S. Ma, Y. Chen, Y. Zhang, N. Yang, M. Xiao, X. Cheng, Z. Gao, *Joule* **2023**, 7, 2361.

[3]   H. Min, M. Kim, S.-U. Lee, H. Kim, G. Kim, K. Choi, J. H. Lee, S. I. Seok, *Science* **2019**, 366, 749.

[4]   J. Jeong, M. Kim, J. Seo, H. Lu, P. Ahlawat, A. Mishra, Y. Yang, M. A. Hope, F. T. Eickemeyer, M. Kim, *Nature* **2021**, 592, 381.

[5]   H. Min, D. Y. Lee, J. Kim, G. Kim, K. S. Lee, J. Kim, M. J. Paik, Y. K. Kim, K. S. Kim, M. G. Kim, *Nature* **2021**, 598, 444.

[6]   M. Kim, G.-H. Kim, T. K. Lee, I. W. Choi, H. W. Choi, Y. Jo, Y. J. Yoon, J. W. Kim, J. Lee, D. Huh, *Joule* **2019**, 3, 2179.

[7]   M. Kim, J. Jeong, H. Lu, T. K. Lee, F. T. Eickemeyer, Y. Liu, I. W. Choi, S. J. Choi, Y. Jo, H.-B. Kim, *Science* **2022**, 375, 302.

[8]   J. Park, J. Kim, H.-S. Yun, M. J. Paik, E. Noh, H. J. Mun, M. G. Kim, T. J. Shin, S. I. Seok, *Nature* **2023**, 1.

[9]   Y.-W. Jang, S. Lee, K. M. Yeom, K. Jeong, K. Choi, M. Choi, J. H. Noh, *Nature Energy* **2021**, 6, 63.

[10]   J. J. Yoo, G. Seo, M. R. Chua, T. G. Park, Y. Lu, F. Rotermund, Y.-K. Kim, C. S. Moon, N. J. Jeon, J.-P. Correa-Baena, *Nature* **2021**, 590, 587.

[11]   Q. Jiang, Y. Zhao, X. Zhang, X. Yang, Y. Chen, Z. Chu, Q. Ye, X. Li, Z. Yin, J. You, *Nature Photonics* **2019**, 13, 460.

[12]   D.-K. Lee, K.-S. Lim, J.-W. Lee, N.-G. Park, *Journal of Materials Chemistry A* **2021**, 9, 3018.

[13]   K.-S. Lim, D.-K. Lee, J.-W. Lee, N.-G. Park, *Journal of Materials Chemistry A* **2020**, 8, 9345.

[14]   J. B. Whitaker, D. H. Kim, B. W. Larson, F. Zhang, J. J. Berry, M. F. Van Hest, K. Zhu, *Sustainable Energy & Fuels* **2018**, 2, 2442.

[15]   W.-Q. Wu, Q. Wang, Y. Fang, Y. Shao, S. Tang, Y. Deng, H. Lu, Y. Liu, T. Li, Z. Yang, *Nature communications* **2018**, 9, 1.

[16]   P. W. K. Fong, H. Hu, Z. Ren, K. Liu, L. Cui, T. Bi, Q. Liang, Z. Wu, J. Hao, G. Li, *Advanced Science* **2021**, 8, 2003359.

[17]   M. Jeong, I. W. Choi, E. M. Go, Y. Cho, M. Kim, B. Lee, S. Jeong, Y. Jo, H. W. Choi, J. Lee, *Science* **2020**, 369, 1615.

[18]   G. Kim, H. Min, K. S. Lee, D. Y. Lee, S. M. Yoon, S. I. Seok, *Science* **2020**, 370, 108.

[19]   C.-H. Chiang, M. K. Nazeeruddin, M. Grätzel, C.-G. Wu, *Energy & Environmental Science* **2017**, 10, 808.

[20]   X. Gong, M. Li, X. B. Shi, H. Ma, Z. K. Wang, L. S. Liao, *Advanced Functional Materials* **2015**, 25, 6671.

[21]   D. Liu, C. J. Traverse, P. Chen, M. Elinski, C. Yang, L. Wang, M. Young, R. R. Lunt, *Advanced Science* **2018**, 5, 1700484.

[22]   A. Wakamiya, M. Endo, T. Sasamori, N. Tokitoh, Y. Ogomi, S. Hayase, Y. Murata, *Chemistry Letters* **2014**, 43, 711.

[23]   G. E. Eperon, S. N. Habisreutinger, T. Leijtens, B. J. Bruijnaers, J. J. van Franeker, D. W. DeQuilettes, S. Pathak, R. J. Sutton, G. Grancini, D. S. Ginger, *ACS nano* **2015**, 9, 9380.

[24]   W. Hui, L. Chao, H. Lu, F. Xia, Q. Wei, Z. Su, T. Niu, L. Tao, B. Du, D. Li, *Science* **2021**, 371, 1359.

[25]   K. Meng, C. Wang, Z. Qiao, Y. Zhai, R. Yu, N. Liu, R. Gao, B. Chen, L. Pan, M. Xiao, *Small* **2021**, 17, 2104165.

[26]   Q. Jiang, L. Zhang, H. Wang, X. Yang, J. Meng, H. Liu, Z. Yin, J. Wu, X. Zhang, J. You, *Nature Energy* **2016**, 2, 1.

[27]   J. Y. Kim, J.-W. Lee, H. S. Jung, H. Shin, N.-G. Park, *Chemical Reviews* **2020**, 120, 7867.

[28]   F. Ma, J. Li, W. Li, N. Lin, L. Wang, J. Qiao, *Chemical science* **2017**, 8, 800.

[29]   D.-K. Lee, Y. Shin, H. J. Jang, J.-H. Lee, K. Park, W. Lee, S. Yoo, J. Y. Lee, D. Kim, J.-W. Lee, *ACS Energy Letters* **2021**, 6, 1821.

[30]   T. Huang, S. Tan, S. Nuryyeva, I. Yavuz, F. Babbe, Y. Zhao, M. Abdelsamie, M. H. Weber, R. Wang, K. N. Houk, *Science advances* **2021**, 7, eabj1799.

[31]   T. B. Song, Z. Yuan, M. Mori, F. Motiwala, G. Segev, E. Masquelier, C. V. Stan, J. L. Slack, N. Tamura, C. M. Sutter-Fella, *Advanced Functional Materials* **2020**, 30, 1908337.

[32]   M. Abdelsamie, T. Li, F. Babbe, J. Xu, Q. Han, V. Blum, C. M. Sutter-Fella, D. B. Mitzi, M. F. Toney, *ACS applied materials & interfaces* **2021**, 13, 13212.

[33]   J. W. Lee, D. H. Kim, H. S. Kim, S. W. Seo, S. M. Cho, N. G. Park, *Advanced Energy Materials* **2015**, 5, 1501310.

[34]   J. K. Jae Sung Yun, Trevor Young, Robert J. Patterson, Dohyung Kim, Jan Seidel, Sean Lim, Martin A. Green, Shujuan Huang, Anita Ho-Baillie, *Advanced Functional Materials* **2018**, 28, 1705363.

[35]   W. S. Yang, B.-W. Park, E. H. Jung, N. J. Jeon, Y. C. Kim, D. U. Lee, S. S. Shin, J. Seo, E. K. Kim, J. H. Noh, *Science* **2017**, 356, 1376.

[36] D.-Y. Son, J.-W. Lee, Y. J. Choi, I.-H. Jang, S. Lee, P. J. Yoo, H. Shin, N. Ahn, M. Choi, D. Kim, *Nature Energy* **2016**, 1, 1.

[37] S. D. Stranks, V. M. Burlakov, T. Leijtens, J. M. Ball, A. Goriely, H. J. Snaith, *Physical Review Applied* **2014**, 2, 034007.

[38] Z. Li, M. Yang, J.-S. Park, S.-H. Wei, J. J. Berry, K. Zhu, *Chemistry of Materials* **2016**, 28, 284.

[39] D. P. McMeekin, G. Sadoughi, W. Rehman, G. E. Eperon, M. Saliba, M. T. Hörantner, A. Haghighirad, N. Sakai, L. Korte, B. Rech, *Science* **2016**, 351, 151.

[40] S. Tan, I. Yavuz, M. H. Weber, T. Huang, C.-H. Chen, R. Wang, H.-C. Wang, J. H. Ko, S. Nuryyeva, J. Xue, *Joule* **2020**, 4, 2426.

[41] D. Meggiolaro, S. G. Motti, E. Mosconi, A. J. Barker, J. Ball, C. A. R. Perini, F. Deschler, A. Petrozza, F. De Angelis, *Energy & Environmental Science* **2018**, 11, 702.

[42] J. S. Yun, J. Kim, T. Young, R. J. Patterson, D. Kim, J. Seidel, S. Lim, M. A. Green, S. Huang, A. Ho‑Baillie, *Advanced Functional Materials* **2018**, 28, 1705363.

[43] J. Lin, M. Lai, L. Dou, C. S. Kley, H. Chen, F. Peng, J. Sun, D. Lu, S. A. Hawks, C. Xie, *Nature materials* **2018**, 17, 261.

[44] I. Ivanov, M. Bolyachkina, M. Mazurin, D. Tsvetkov, V. Sereda, A. Y. Zuev, *Thermochimica Acta* **2017**, 658, 24.

[45] E. L. Unger, A. R. Bowring, C. J. Tassone, V. L. Pool, A. Gold-Parker, R. Cheacharoen, K. H. Stone, E. T. Hoke, M. F. Toney, M. D. McGehee, *Chemistry of Materials* **2014**, 26, 7158.

[46] A. E. Williams, P. J. Holliman, M. J. Carnie, M. L. Davies, D. A. Worsley, T. M. Watson, *Journal of Materials Chemistry A* **2014**, 2, 19338.

[47] Z. Deng, X. Lu, Z. Wen, S. Wei, Q. Zhu, D. Jin, X. Shi, W. Guo, *RSC advances* **2014**, 4, 12266.

[48] **2009**.

[49] L. Shi, M. P. Bucknall, T. L. Young, M. Zhang, L. Hu, J. Bing, J. Kim, T. Wu, N. Takamure, D. R. McKenzie, *Science* **2020**, 368.

[50] E. J. Juarez-Perez, Z. Hawash, S. R. Raga, L. K. Ono, Y. Qi, *Energy & environmental science* **2016**, 9, 3406.

[51] M. Lyu, N.-G. Park, *Solar RRL* **2020**, 4, 2000331.

[52] S. Tan, T. Huang, I. Yavuz, R. Wang, T. W. Yoon, M. Xu, Q. Xing, K. Park, D.-K. Lee, C.-H. Chen, *Nature* **2022**, 605, 268.

[53]   T.-B. Song, Z. Yuan, F. Babbe, D. P. Nenon, E. Aydin, S. De Wolf, C. M. Sutter-Fella, *ACS Applied Energy Materials* **2020**, 3, 2386.

[54]   J. Mooney, P. Kambhampati, *The journal of physical chemistry letters* **2013**, 4, 3316.

[55]   M. Abdelsamie, K. Zhao, M. R. Niazi, K. W. Chou, A. Amassian, *Journal of Materials Chemistry C* **2014**, 2, 3373.

[56]   K. Wang, R. Z. Liang, J. Wolf, Q. Saleem, M. Babics, P. Wucher, M. Abdelsamie, A. Amassian, M. R. Hansen, P. M. Beaujuge, *Advanced Functional Materials* **2016**, 26, 7103.

[57]   J. P. Perdew, A. Ruzsinszky, G. I. Csonka, O. A. Vydrov, G. E. Scuseria, L. A. Constantin, X. Zhou, K. Burke, *Physical review letters* **2008**, 100, 136406.

[58]   P. E. Blöchl, *Physical review B* **1994**, 50, 17953.

[59]   G. Kresse, J. Furthmüller, *Physical review B* **1996**, 54, 11169.

Atmospheric humidity control during fabrication process crucially influences the phase formation and stability of formamidinium perovskites. This work reveals that controlled humidity during fabrication process is a key to achieving reproducible fabrication of high-quality and stable perovskite films. Thus, precise humidity management is essential to ensure the reproducible, efficient, and stable perovskite solar cells.

K. Park, S. Tan, T. Kodalle, D.-K. Lee, M. Abdelsamiee, J.-S. Park, J.-H. Lee, S.-K. Jung, J. H. Ko, N.-G. Park, C. M. Sutter-Fella,*, Y. Yang,*, J.-W. Lee*

Atmospheric humidity underlies irreproducibility of formamidinium lead iodide perovskites

ToC figure